

Hidden Complexity in the Chemistry of Ammonolysis-Derived “ γ - Mo_2N ”: An Overlooked Oxynitride Hydride

Shobhit A Pandey, Chi Zhang, Daniah H. Ibrahim, Elise A Goldfine, Jill K. Wenderott, Roberto dos Reis, Rick L. Paul, Ioannis Spanopoulos, Mercuri Kanatzidis, Michael J. Bedzyk, Vinayak P. Dravid,* Gabriela B. González,* and Sossina M. Haile*



Cite This: *Chem. Mater.* 2021, 33, 6671–6684



Read Online

ACCESS |



Metrics & More

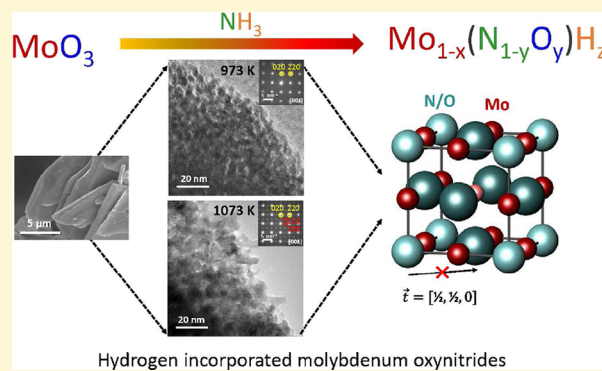


Article Recommendations



Supporting Information

ABSTRACT: Molybdenum nitrides have been employed in a variety of applications. For use in catalysis, the cubic γ phase with the nominal stoichiometry Mo_2N and the space group $Fm\bar{3}m$ is typically prepared by high-temperature reaction of MoO_3 with NH_3 . The literature presents conflicting reports of the possible presence of residual oxygen from typical ammonolysis reactions and whether such species influence the crystal structure and morphology. With the aim of resolving these open questions, a comprehensive study of the chemistry, crystal structure, and electronic structure of molybdenum nitride materials prepared by ammonolysis has been undertaken here, with particular focus on the role of reaction temperature. Ammonolysis of MoO_3 was carried out at 973 and 1073 K and yielded single-phase cubic products. Using electron energy loss spectroscopy (EELS), X-ray photoelectron spectroscopy (XPS), thermogravimetric analysis, prompt gamma-ray neutron activation analysis, and combustion analysis, significant concentrations of oxygen and, to a lesser extent, hydrogen were found in both materials. The crystal structure of each phase was refined by Rietveld analysis using combined synchrotron X-ray diffraction and neutron diffraction data. The structures were found to be derivatives of the B1 rock salt (halite) structure, as is often reported for “ γ - Mo_2N .” However, both materials adopt the space group $Pm\bar{3}m$, as opposed to the typically presumed space group of $Fm\bar{3}m$, and both have much higher anion content than implied by the stoichiometry Mo_2N . Ordering of cation vacancies and of anion species is responsible for the loss of the translational symmetry expected for the space group $Fm\bar{3}m$. X-ray absorption spectroscopy studies, along with the EELS and XPS results, showed the Mo oxidation state to be diminished with higher temperature synthesis, consistent with the retention of a lower concentration of anions and in particular oxygen. The difficulty in differentiating oxygen and nitrogen and the impossibility of detecting hydrogen by X-ray and electron diffraction methods, especially in the presence of the heavy element Mo, have likely inhibited accurate identification of $\text{Mo}_{1-x}(\text{N}_{1-y}\text{O}_y)\text{H}_z$ as the product of MoO_3 ammonolysis. The findings reported here offer a critical assessment for understanding the properties of molybdenum “nitrides” in electronic and catalytic applications.



1. INTRODUCTION

Molybdenum nitrides have received significant attention due to their excellent and tunable mechanical, electronic, thermal, catalytic, and magnetic properties.^{1,2} A range of synthetic approaches have been employed to produce materials within this class. In studies in which the physical and electronic properties are of interest, thin film approaches such as sputtering and physical vapor deposition are common.² When the catalytic,^{3–7} electrocatalytic,^{8–15} and electrochemical^{16–18} properties are instead targeted, temperature-programmed reaction of oxide precursors with ammonia (ammonolysis) is often pursued to generate materials with a high specific surface area.^{19–21} Materials produced via such a route are the subject of the present work.

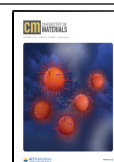
Successful synthesis of the target molybdenum nitride phase, most commonly the B1-type γ phase, from the ammonolysis

reaction is typically presumed on the basis of the agreement of the experimental X-ray diffraction (XRD) pattern with that in the International Center for Diffraction Data database.²² In a handful of studies, it has been recognized that, despite displaying a readily recognized diffraction pattern, the product of this reaction can, in fact, retain a substantial oxygen content such that the material may be more appropriately considered a molybdenum oxynitride.^{23–26} In particular, Lyutaya²⁶ reported that, of the anions in a sample produced by ammonolysis of

Received: February 20, 2021

Revised: August 10, 2021

Published: August 26, 2021



MoO₃ at 973 K, ≈28 mol % were oxygen atoms, whereas Gouin et al.²³ reported that 17 mol % of the anions were oxygen atoms after synthesis under similar conditions. Furthermore, as shown by Kreider et al. for the example of oxygen reduction activity, the extent of oxygen uptake can profoundly impact properties.²⁷ In parallel, some studies have revealed that bulk hydrogen uptake can also occur in these materials either during the ammonolysis itself²⁴ or by post-synthesis treatment.^{7,28} Alternative synthesis routes, such as the direct reaction of Mo and N₂ or nitride film growth under high vacuum conditions, may inherently limit, without entirely precluding, the possibility of incorporation of foreign species (O and H).²⁶ The crystallographic features of the phases resulting from these nominally oxygen-free synthesis conditions and from bulk ammonolysis are surprisingly similar. This similarity is likely the reason the products of ammonolysis have often been judged to be strictly nitrides.

A rather intriguing feature of the crystal chemistry of the γ phase of molybdenum nitride is the apparently high concentrations of anion vacancies. The phase is typically described as having a stoichiometry of Mo₂N, with nitrogen atoms randomly distributed over one half of the available octahedral anion sites of the B1 structure.²⁸ Although deviations from the 2:1 stoichiometric ratio are rather widely recognized,²⁹ the extent to which the true stoichiometry may differ from this idealized value is not well-established. From an electron-counting perspective, there is little reason to expect a stoichiometry of Mo₂N, and indeed, atomistic computational studies have suggested the existence of several ordered phases across the Mo–N system.³⁰ Troitskaya and Pinsker³¹ reported the existence of Mo₃N₂ (obtained from ammonolysis of Mo films), a phase richer in anions than the standard Mo₂N stoichiometry. This phase was considered to be distinct from the conventional γ phase due to the presence of vacancies on both anion and cation sites, with cation site vacancies ordered such that the symmetry was lowered from $Fm\bar{3}m$ to $Pm\bar{3}m$. The occurrence of a molybdenum nitride phase of the space group $Pm\bar{3}m$ that is similarly rich in anions relative to “Mo₂N” has also been reported from ammonolysis of MoO₃. Specifically, Tagliazucca et al.³² reported a primitive cubic phase of stoichiometry of Mo_{3.2}N_{2.7} when the synthesis was carried out at 1073 K. The conventional *higher* symmetry $Fm\bar{3}m$ phase was obtained from ammonolysis at a *lower* reaction temperature of 923 K. This surprising behavior (of a decrease in symmetry on increasing synthesis temperature) was not explained. Overall, these factors indicate that, while the stoichiometry and chemistry of “ γ -Mo₂N” are at first glance rather simple, the material is in fact chemically quite complex, with variable anion/cation stoichiometry, possible ordering at high temperature, and unknown solubility of oxygen and hydrogen.

In this work, we undertake a comprehensive chemical, crystallographic, electronic, and morphological study of molybdenum nitride phases prepared by ammonolysis of MoO₃ at two temperatures, 973 and 1073 K. We first characterize the products using electron energy loss spectroscopy (EELS) in a scanning/transmission electron microscope (S/TEM), X-ray photoelectron spectroscopy (XPS), X-ray absorption spectroscopy (XAS), thermogravimetric analysis (TGA), prompt gamma-ray neutron activation analysis (PGAA), and combustion analysis to establish the chemical compositions of the distinct phases produced. Using these compositions to inform models, the structure of each phase is

determined by Rietveld refinement using combined synchrotron XRD and neutron diffraction (ND) data. ND is particularly well suited to the study of molybdenum oxynitrides because N and O, with respective scattering lengths of 9.36 and 5.803 fm,³³ can be differentiated, and the pattern is not dominated by Mo (with a neutron scattering length of 6.715 fm), as it is in XRD and electron diffraction. The crystallographic characterization is supplemented by electron microscopy, surface area analysis, and pycnometry for morphological and physical evaluation. These studies reveal that both materials contain considerable concentrations of oxygen, along with some hydrogen, in addition to the primary molybdenum and nitrogen components. Furthermore, *both* materials, one obtained at 973 K and the other at 1073 K, crystallize in a structure of the space group $Pm\bar{3}m$, and both contain substantial concentration of cation vacancies. They are readily distinguished by the non-negligible X-ray and electron diffraction intensities of peaks with mixed even and odd h , k , and l indices in the compound synthesized at 1073 K, peaks that are expected to be absent due to lattice centering in the space group $Fm\bar{3}m$. The clarification provided here of the crystal chemical features of the product of MoO₃ ammonolysis provides an essential grounding for understanding the structure–property relations in this widely employed material.

2. RESULTS

2.1. Physical and Chemical Analysis. The nitridation process converted the light green oxide, which consisted of platelet-shaped crystallites tens of micrometers in length, into a black powder with metallic luster, consistent with the metallic nature of molybdenum nitrides (Figure S1). The characteristics of the resulting materials, where A700 refers to the product of reaction at 973 K and A800 to the product of reaction at 1073 K, are summarized in Table 1, and the representative electron microscopy images are presented in Figure 1. In Table 1 and hereafter, a number in parentheses following a reported measured value indicates the uncertainty in the final digit(s) and is given in the range from 1 to 9, with the exception of crystallographic parameters, for which the uncertainty is reported in the range from 2 to 19. As evident from Figure 1, the reaction generally preserved the original shape of the micron-sized oxide. Despite the apparently smooth particle morphologies, the specific surface areas of the nitrated products were 135(2) and 47.7(3) m² g⁻¹ for A700 and A800, respectively (Table 1), much higher than the 1–2 m² g⁻¹ surface area of the precursor MoO₃. Upon repetition of the synthesis and Brunauer–Emmett–Teller (BET) characterization, respective values of 111.9(7) and 70.3(3) m² g⁻¹ were obtained. An increase in surface area from the precursor to product is common during ammonolysis of MoO₃ at 973 K and is attributed to the topotactic nature of this pseudomorphic transformation with a concomitant decrease in density.^{6,19,34} Slight differences in features are evident between the two materials in the SEM images in the form of large pores and depressions on the surface of A800 (Figure 1b), which are absent in A700 (Figure 1a).

The TEM images reveal a high level of nanoscale porosity within the macroscopic particles, accounting for the high specific surface area. The images further show A800 (Figure 1d) to have a generally coarser microstructure than A700 (Figure 1c). Pores in A700 separate crystalline regions that are 7–8 nm in size, whereas the crystalline regions between pores in A800 span 10–15 nm. These dimensions broadly match the

Table 1. Summary of the Results of Characterization of Materials produced by Ammonolysis of MoO₃ at 973 (A700) and 1073 K (A800)^a

	A700	A800
Chemical Analysis		
EELS analysis		
elements detected	Mo, N, and O	Mo, N, and O
Mo edge peak	398.4(4) eV	396.8(4) eV
N edge peak	401.6(4) eV	400.4(4) eV
thermal XPS spectra		
elements detected	Mo, N, and O	Mo, N, and O
binding energy (BE) for Mo ^{δ+}	229.3(1) eV	228.9(1) eV
combustion analysis		
absolute N content, as-synthesized	11.1(3) mass %	10.1(3) mass %
absolute N content, surface-desorbed	10.1(3) mass %	9.2(3) mass %
absolute H content, as-synthesized	0.8(3) mass %	0.4(3) mass %
absolute H content, surface-desorbed	0.4(3) mass %	0.1(3) mass %
PGAA analysis		
Mo/N atomic ratio	1.05(3)	1.13(3)
Mo/H atomic ratio	1.19(3)	2.53(6)
Deduced from TGA		
atomic fraction O/(O + N)	0.18–0.28	0.13–0.22
atomic anion/cation ratio	0.97–1.14	0.82–0.93
Structural Characterization		
BET measurement		
surface area	135(3) m ² g ⁻¹	47.7(3) m ² g ⁻¹
pore size(s)	3.6(1) nm	3.4(1) nm, 8.7(1) nm (bimodal)
pycnometry: measured density		
	5.0783(1) g cm ⁻³	5.6307(1) g cm ⁻³
Diffraction Corefinement Results		
crystallographic formula	Mo _{0.775(2)} (N _{0.75} O _{0.25})	Mo _{0.790(1)} (N _{0.729(5)} O _{0.062(1)})
theoretical density	8.06(2) g cm ⁻³	7.68(1) g cm ⁻³
Mo/N molar ratio	1.033(3)	1.084(1)
N	11.82(3) mass %	11.73(1) mass %
Mo	83.7(2) mass %	87.1(1) mass %
atomic fraction O/(O + N)	0.25	0.078(1)
atomic anion/cation ratio	1.290(4)	1.000(1)
lattice parameter	4.18426(8) Å	4.22154(7) Å

^aEstimated uncertainty in the final digit(s) of the reported values is provided in parentheses. See the text for methods of uncertainty determination.

crystallite sizes implied from the peak broadening in the diffraction patterns (Figure 2), 7.1(1) and 9.3(2) nm, for A700 and A800, respectively. The values for these specific samples used in structure refinement were in line with the respective averages of 7.2(2) and 9.9(6) nm obtained from the analysis of multiple syntheses (Figure S2). Rather remarkably, the large, mesoporous particles visible in the SEM and TEM images of both A700 and A800 are single crystals, as evident from the

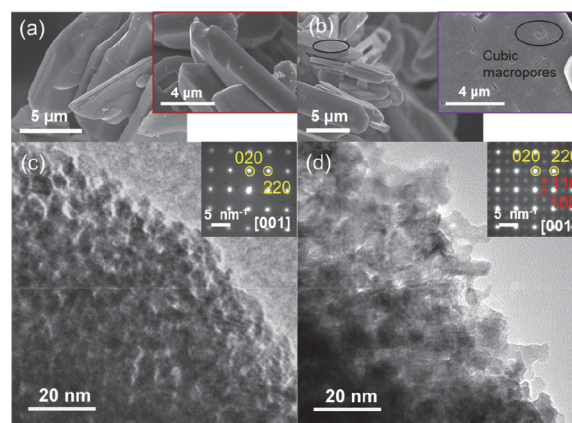


Figure 1. Electron microscopy images of the products of ammonolysis of MoO₃: (a,c) Scanning and transmission electron images, respectively, of A700 and (b,d) analogous respective images of A800. Insets in (a) and (b) show enlarged SEM images, whereas those in (c,d) show SAED patterns. Large crystallites in both materials are mesoporous single crystals, with nanoscale crystalline regions (7–8 nm in A700 and 10–15 nm in A800) retaining crystallographic registry over the length scale of the original trioxide precursor particle. The A800 material additionally features pores that are tens of nanometers on edge. The SAED indexing and nanoscale features agree with the XRD analysis.

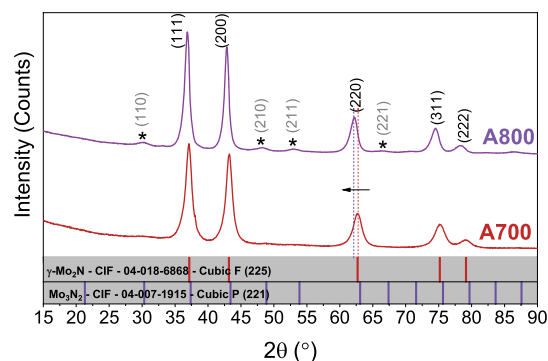


Figure 2. Representative lab XRD patterns of A700 (lower) and A800 (upper) collected with Cu K α radiation ($\lambda = 1.5406$ Å). Diffraction peaks of mixed hkl parity, required to be absent for a face-centered cubic lattice, have finite intensity in the pattern of A800. The patterns are further differentiated by the narrower peaks, indicative of a larger crystallite size, and the larger lattice constant of the A800 material.

TEM selected area electron diffraction (SAED) patterns (insets of Figure 1c,d). These were obtained using a selected area aperture with an effective diameter of up to ≈ 600 nm, and every region within the same particle (several micrometers in lateral dimensions) exhibited the identical diffraction pattern. These patterns reveal the cubic nature of the two materials and also show the crystal structures to be distinct. Beyond occasional detection of the isolated amorphous molybdenum oxide particles, no impurity phases were revealed by the TEM studies.

In agreement with the electron diffraction result, the lab XRD patterns (Figures 2 and S2) of the A700 and A800 materials match, at least to a first approximation, the respective patterns reported for γ -Mo₂N (JCPDS no. 04-018-6868, space group $Fm\bar{3}m$) and for Mo₃N₂ (JCPDS no. 04-007-1915, space group $Pm\bar{3}m$). The peaks that are systematically absent from the pattern of the A700 material (h , k , and l mixed even and

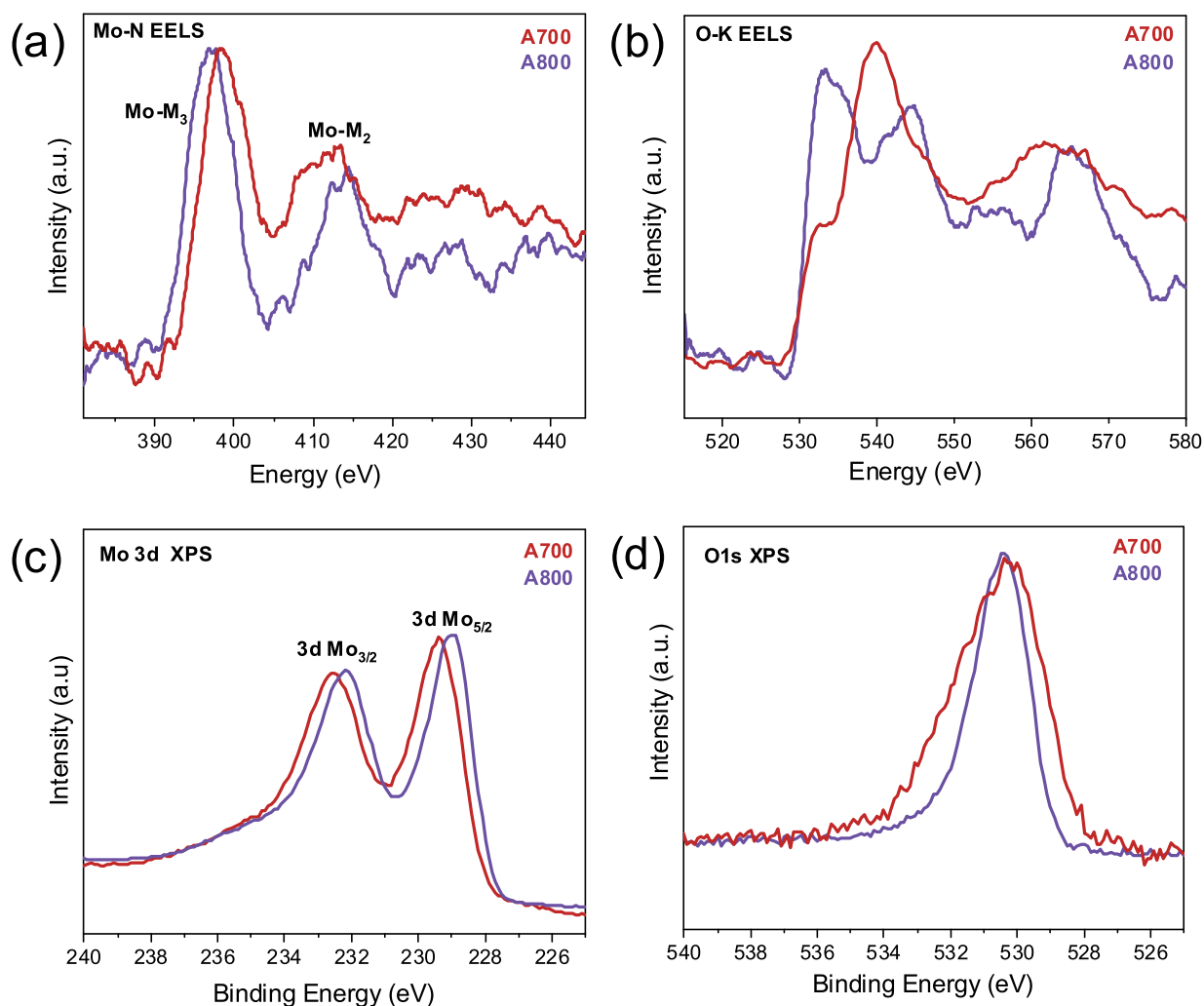


Figure 3. Spectroscopy studies of the products of ammonolysis of MoO_3 : (a,b) EELS measurements and (c,d) XPS measurements, with spectra for A700 in red and those for A800 in purple. Vertical scales of the A700 and A800 scans were normalized to match the backgrounds and the maximum peak heights. Features of the electronic structure about the Mo $M_{2,3}$ or Mo 3d edge are shown in (a,c), whereas those about the O–K or O 1s edge are shown in (b,d). The oxygen ELNES (b) reveals that bulk oxygen is retained in both materials, whereas the electronic structure about Mo (a,c) reveals that Mo is more reduced after ammonolysis at 1073 K than that at 973 K.

odd) are weak in the pattern of A800 but are nevertheless detectable, consistent with the space group characteristics. The SAED patterns collected along the $[001]$ zone axis for both materials similarly show nonzero intensity for peaks of mixed parity in the A800 material (inset of Figure 1d), whereas this class of peaks is completely absent in the pattern of the A700 material (inset of Figure 1c). Furthermore, the A800 lattice parameter is measurably larger than that of the A700 material. The present results are in agreement with the observations of Tagliazucca et al.,³² who reported that the $Pm\bar{3}m$ superstructure peaks appear when ammonolysis is carried out at 1073 K. Here, the weak superstructure peaks were always detected in materials synthesized at an ammonolysis temperature of 1073 K, while careful examination of the patterns of several A700 materials (Figure S2b), indicated that even after ammonolysis at 973 K, superstructure peaks can occasionally be detected. In addition to being extremely weak, these peaks were found, in all cases, to be much broader than the substructure peaks, suggesting that they could be easily overlooked.

The phase identification based on the diffraction data, which generally indicated consistency with the pattern of “ Mo_2N ,”

could easily be interpreted to signify that only Mo and N are present in the materials synthesized here. However, the EELS measurements (Figure 3) unequivocally revealed the presence of oxygen within the bulk of the ≈ 50 nm thick particles, along with N and Mo. In particular, the distinctiveness of the features of the O_K energy loss near-edge structure (ELNES) spectra, especially those of the A700 material, demonstrates that the oxygen detected cannot originate from either surface oxides or the gas phase (Figure S3).³⁵ Furthermore, as evident from the high-resolution TEM imaging and SAED, the particles are free from structurally distinct surface phases (a surface oxide would be expected to be amorphous).³⁶ In the case of the XPS data (Figure 3), which, unlike EELS, are dominated by the surface region of the material, the possibility of residual surface species of oxygen and/or H_2O remaining after thermal treatment at 523 K and contributing to the response cannot be ruled out. However, the high intensity of the measured O 1s signal, with an integrated intensity approximately one-third of that of the Mo signal, suggests that bulk oxygen has been detected in addition to that at the surface. Quantification of the composition by XPS was precluded by the presence of surface species (as revealed by the TGA studies), along with the

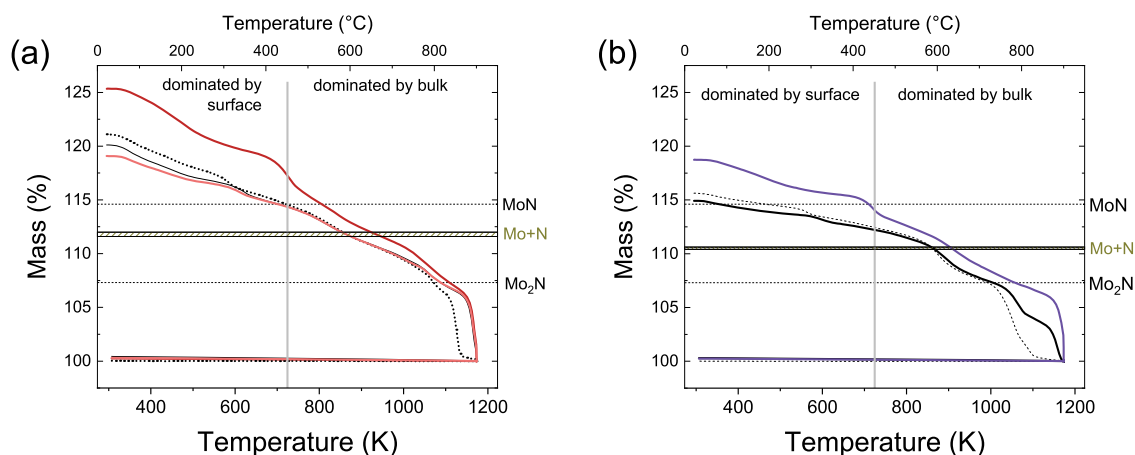


Figure 4. TGA mass loss profiles under dilute hydrogen (solid lines: 3% H₂, dashed lines: 7% H₂) for (a) A700 and (b) A800 materials obtained using samples 50–75 mg in mass and a heating rate of 5 K min⁻¹. Data shown include those from samples showing maximum and minimum mass losses under 3% H₂. The masses are normalized to 100% upon completion of reduction in recognition of the variable surface mass content. Horizontal lines indicate the masses of ideal Mo₂N and ideal MoN and the mass range implied by the combustion analysis determination of the N content. A change in the gas atmosphere from 3% to 7% H₂ (with profiles recorded using the material from the same synthesis batch, black curves) has a negligible impact on the mass loss behavior at temperatures below ≈1023 K.

overall roughness of the samples and the overlap of N and Mo peaks.

Significantly, the electronic states of all three elements, Mo, O, and N, differ noticeably between the two materials, as revealed by the EELS edge energies and XPS binding energies summarized in Table 1. The white line maximum of Mo in the Mo_{M2,3} ELNES spectrum of A800 is shifted to lower energy than in A700 (Figure 3a), as is the doublet peak in the Mo 3d region of the XPS spectrum (Figure 3c). These features indicate that Mo is more reduced after ammonolysis at 1073 K than at 973 K. In the XPS results, the Mo^{δ+} species accounted for 68 and 50% of the total Mo 3d intensity in the spectra of A700 and A800, respectively (Figure S4 and Table S1), outweighing contributions from Mo⁶⁺ and Mo⁴⁺. Thus, the Mo^{δ+} signature was taken to reflect the Mo in the bulk. The Mo^{δ+} peak positions of 229.3(1) eV (A700) and 228.9(1) eV (A800) correspond in both materials to an Mo oxidation state of ≈+3, according to the correlation between the BE and oxidation state reported by Choi and Thompson.³⁷ The Mo⁴⁺ and Mo⁶⁺ species are attributed to residual surface species, likely trapped at the interfaces between individual particles in the pressed compacts. A very slight shift toward higher energy in the X-ray absorption near-edge spectroscopy (XANES) spectra is also visible (Figure S5), but in this case, the effect is almost within the margin of experimental error. For both materials, the position of the adsorption edge indicates a Mo oxidation state lying between the +4 value of MoO₂ and the 0 value of metallic Mo. In the EELS measurements, which, as noted, reflect the oxygen in the bulk, a dramatic difference in spectral features in the oxygen region of A700 and A800 is evident. This result suggests significant differences in the near-neighbor environments about oxygen in the two materials. The EXAFS measurements indicate an analogous dramatic difference in the near-neighbor environment about Mo (Figure S6). In the XPS spectra (Figure 3d), a slight broadening of the O 1s peak is evident for the A700 material. However, the overall similarities between the two materials are consistent with an oxygen signal highly influenced by surface species. In sum, the spectroscopic studies reveal the presence of bulk oxygen and demonstrate that Mo in A800 is slightly more reduced than

that in A700 and that the local structure differs substantially between the two.

The TGA profiles for the complete reduction experiments (Figure 4) revealed nearly continuous mass loss from the initiation of the thermal treatment to approximately 1123 K, at which a sharp, final mass loss occurred. The representative profiles reflect the span of behaviors observed for the two respective materials. The total mass loss ranged from 19(2)% to 25(3)% of the Mo mass for A700 materials, whereas it ranged from 15(2)% to 19(2)% for A800. The profiles do not display any obvious plateaus that could enable definitive distinction between features reflecting the loss of mass from the surface vs that from the bulk. Nevertheless, it is immediately evident that the mass loss is inconsistent with materials of ideal bulk composition Mo₂N or even, in the case of A700, MoN. That is, the losses are substantially greater than what Mo₂N or MoN would yield. For example, for the A700 material to correspond to the ideal stoichiometry of Mo₂N, all of the mass loss up to ≈1093 K would have to be due to surface species. In the case of A800, this temperature is slightly lower, ≈1023 K, but is still very high for bulk stability. The in situ diffraction experiments under H₂ (Figure 5) revealed the changes in bulk diffraction features, beyond simple thermal expansion, initiated at ≈723 K, indicating that the bulk is anion-rich relative to Mo₂N. On heating beyond 723 K, cell contraction was observed for both A700 and A800, along with a decline in the I(200)/I(111) peak intensity ratio (Figure S7). The significant difference in the lattice parameter between A700 and A800, well outside of the range of experimental uncertainty, further underscores the distinction between the two materials. With mass losses below ≈723 K attributed largely to surface species, it is evident that such species constitute a greater proportion of the mass of A700 than of A800, consistent with the higher specific surface area of the former.

Turning to the quantitative chemical characterization, the combustion analysis indicated absolute N contents in as-synthesized A700 and A800 of 11.1(3) and 10.1(3) mass %, respectively (Table 1), as averaged over measurements of three distinct samples. After surface desorption, the N contents

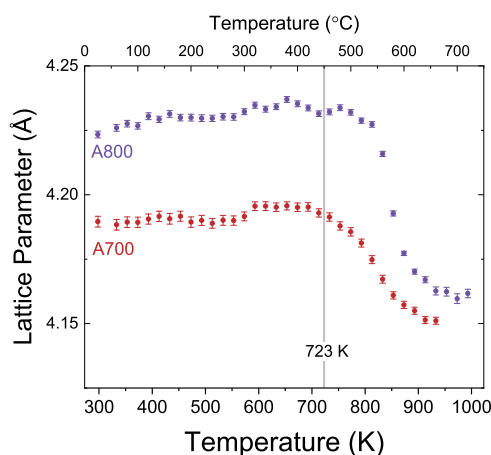


Figure 5. Lattice constant of A700 and A800 materials (as indicated) upon heating under 7% H₂ (balance He) at a heating rate of 2 K min⁻¹. Under these conditions, both materials are fully transformed to Mo at 1053 K. The onset of apparent cell contraction at ≈723 K is taken to be indicative of bulk changes in the composition. This coincides with a slight decline in the intensity ratio of the (200) to (111) peaks shown in Figure S7.

decreased slightly to 10.1(3) and 9.2(3) mass %, respectively. The total mass (of Mo and N) implied by the combustion analysis is indicated on the TGA profiles, where the range results from the range in initial masses relative to the final, Mo-only mass. Presuming that the treatment under Ar at 673 K has removed the majority of the surface species, the result along with the total mass change up to this temperature indicates that 30–40% of the mass lost by desorption from A700 is due

to nitrogen. In the case of A800, the proportion is 40–55%. Thus, residual NH₃ accounts for a significant, but not dominant, fraction of the surface species in the as-synthesized material. The PGAA analysis (Figure S8 and Table 1) revealed Mo/N molar ratios of 1.05:1 and 1.13:1 for as-synthesized A700 and A800, respectively, which are entirely consistent with the combustion analysis. The PGAA additionally revealed high hydrogen concentrations in both as-synthesized materials, particularly the A700 material. The result is consistent with the combustion analysis, which, although close to the hydrogen detection limit, suggests a higher concentration of H in A700 than in A800. While some of the difference is likely due to the differences in the quantities of surface-adsorbed species, NH₃ and possibly H₂O (Figure 4), the difference is too large to be accounted for in this way. Thus, it can be concluded that A700 and likely also A800 retain hydrogen in the structure.

The most significant feature of the chemical analyses is the clear evidence that the sum of the Mo and N contents does not account for the total sample mass. This can be seen in TGA profiles, in which this sum lies below the measured mass curve until a temperature of about 923 K in the case of A700 and of about 873 K for A800, well into the regime at which bulk changes occur. This behavior immediately implies that some other species is present in the materials. This species is presumably oxygen, as the mass of H as determined by PGAA, the only other candidate, is too small to account for this difference. Taking, on the basis of the in situ XRD results, a temperature of 723 K to be a reasonable temperature for delineating between bulk and surface loss and using the nitrogen content measured by combustion analysis of the surface desorbed materials, it is possible to estimate the bulk

Table 2. Atomic Coordinates, Site Occupancies, and Isotropic Displacement Factor Coefficients for Molybdenum Oxynitride-Hydrides, A700 and A800, Obtained from Rietveld Analysis Using Combined X-ray Synchrotron and Neutron Time-of-Flight Powder Diffraction Data^a

	A700 Mo _{0.775(2)} (N _{0.75} O _{0.25})	A800 Mo _{0.790(1)} (N _{0.729(5)} O _{0.062(1)})
space group	<i>Pm</i> $\bar{3}$ <i>m</i>	<i>Pm</i> $\bar{3}$ <i>m</i>
lattice parameter (Å)	4.18426(8)	4.22154(7)
site 1a, <i>m</i> $\bar{3}$ <i>m</i> , 0 0 0	Mo(1)	Mo(1)
occupancy	0.559(4)	1 [fixed]
Uiso (10 ² Å ²)	0.509(8)	0.785(8)
site 3c, 4/ <i>mmm</i> , 0 1/2 1/2	Mo(2)	Mo(2)
occupancy	0.8470(15)	0.7206(12)
Uiso (10 ² Å ²)	0.509(8) [constrained] ^b	0.785 (8) [constrained] ^b
site 1b, <i>m</i> $\bar{3}$ <i>m</i> , 1/2 1/2 1/2	O(1)	N(1)
occupancy	1 [fixed]	0.162(4)
Uiso, 10 ² Å ²	0.781(4)	0.531(6)
coord. no. (6 × 3c)	5.1	4.3
site 3d, 4/ <i>mmm</i> , 1/2 0 0	N(2)	N(2)/O(2)
occupancy [total fixed to 1]	1 [fixed]	0.918(5)/0.082(5)
Uiso (10 ² Å ²)	0.781(4) [constrained] ^b	0.531 [constrained] ^b
coord. no. (4 × 3c + 2 × 1a)	4.5	4.9
goodness of fit	1.33	1.78
residual wRp (%)		
NB1	3.41%	6.28%
NB2	3.82%	7.40%
X-ray	12.71%	14.88%
combined	5.95%	9.55%

^aEstimated standard deviation in last digit(s) of refined parameters provided in parentheses. Following recommended practices of the International Union of Crystallographers,³⁸ uncertainty values are reported in the range from 2 to 19. ^bDisplacement parameters of all anions and cations in a single structure constrained to equal one another.

oxygen content. For A700, the result is 2.5–4.5 mass %, whereas for A800, it is 1.6–3.0 mass %. These values translate into anion molar fractions (relative to the total anion content) of 0.18–0.28 and 0.13–0.22, respectively (Table 1). From this, values for total anion to cation ratios can be deduced and are also provided in Table 1. Because of the large uncertainty in differentiating between bulk and surface mass loss, more important than the absolute values is the clear evidence that A700 is anion rich relative to A800.

A final piece of chemical information was provided by the measured densities using pycnometry, found to be 5.0783(1) and 5.6307(1) g cm⁻³ for the specific A700 and A800 samples, respectively, for which structure refinement was performed. These values are far lower than the expected density of 9.34 g cm⁻³ for ideal γ -Mo₂N, and the discrepancy is even greater for ideal rock salt MoN, with an expected density of 9.98 g cm⁻³. Furthermore, the measured densities showed a wide range of values, although they were consistently larger for A800 than for A700 materials and always smaller than the values expected for ideal γ -Mo₂N. The variation (within a given material class, A700 or A800) was found to be correlated to the MoO₃ precursor source and uncorrelated to the lattice parameter (Figure S9). This result suggests that a large concentration of closed pores or possibly crystallographic vacancies, which would be inaccessible to pycnometry and (in the case of closed pores) highly dependent on the precursor morphology, contribute to the low density. Significantly, although the absolute densities of A800 materials are systematically greater than those of the A700 materials, the mass per unit cell volume is greater in the latter as a consequence of the smaller lattice constant. Thus, the internal porosity and/or vacancy concentration must be greater in A800 than in A700.

2.2. Structure Determination. With the above insights into the chemical compositions of A700 and A800, in particular the presence of oxygen, structural refinements to simultaneously fit to the synchrotron XRD and time-of-flight (TOF) ND data were undertaken. A summary of the refinement results is provided in Table 2, and the measured and final calculated patterns are presented in Figure 6, with the difference patterns presented in Figure S10. Direct comparisons of the experimental patterns of the two materials are provided in Figure S11. Two key features are evident directly from the diffraction data. First, the ND patterns, particularly those from A700, show significant background intensity, which is readily attributed to incoherent scattering from the hydrogen in the materials. Second, all of the patterns (both X-ray and neutron and from both materials) indicate nonzero intensity of the (110), (210), and (211) peaks. In the X-ray synchrotron data, these peaks are rather weak and broad, especially in A700, but they nevertheless have nonzero intensity. Detection of these mixed *hkl* parity peaks immediately indicates that the lattice is not face-centered cubic for either material. Ultimately, the best fits were obtained using the space group $Pm\bar{3}m$ for both materials. The low symmetry of A700 is particularly surprising as this material appeared consistent with the space group $Fm\bar{3}m$ by lab XRD and SAED, a typical result in the literature.

The distinction between space groups $Pm\bar{3}m$ and $Fm\bar{3}m$ in the present context lies largely in the chemical identities of the species residing on the pairs of sites, 1a, 3c and 1b, 3d (Figure 7). In $Fm\bar{3}m$, the species within each pair are identical such that the translational symmetry of the FCC lattice (+0 +1/2 +1/2; +1/2 +0 +1/2; and +1/2 +1/2 +0) is obeyed. The

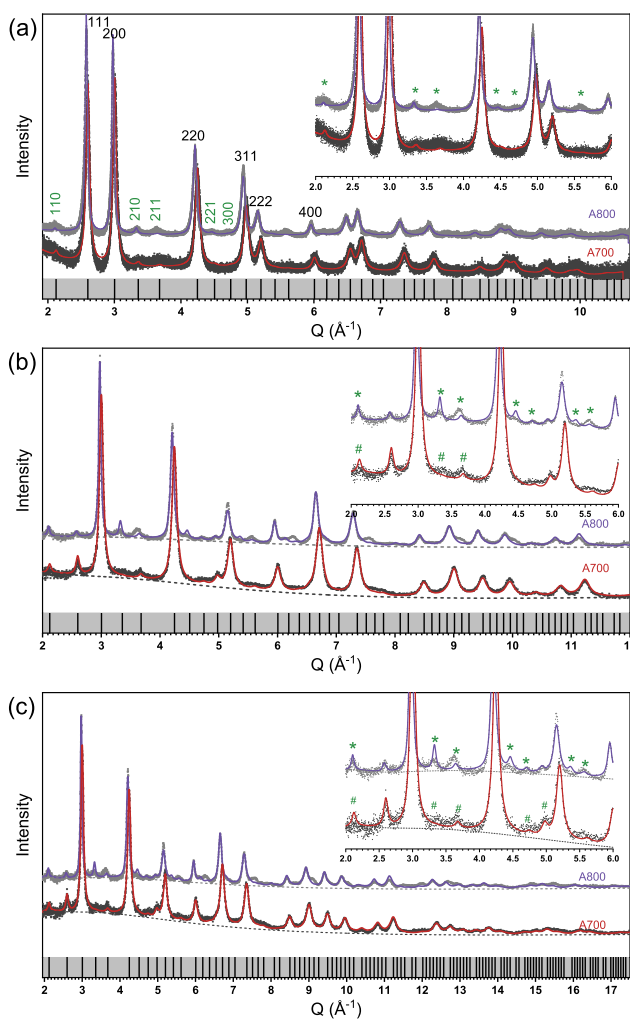


Figure 6. Measured and calculated diffraction patterns, the latter from corefinement of the structures of A700 and A800 materials: (a) synchrotron, (b) NBI, and (c) NB2 data. For ease of comparison, data are presented as functions of Q (\AA^{-1}). Measured data are shown as dots, and calculations as lines. Insets in each figure show a zoomed-in region from 2.0 to 6.0 Q (\AA^{-1}), with prominent superstructure peaks in A800 marked in * and those of A700 marked in #. A700 shows superstructure peaks only in NPD, whereas for A800, superstructure peaks are found in both XRD and NPD patterns.

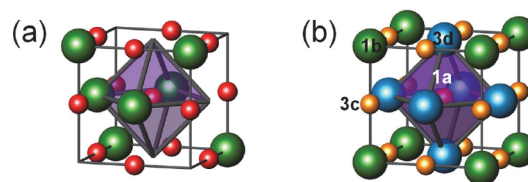


Figure 7. Structure of (a) conventional “ γ -Mo₂N” with the space group $Fm\bar{3}m$ and (b) the Mo–O–N–H materials identified in this work with the space group $Pm\bar{3}m$. The structures of both the A700 and A800 materials are represented in (b), and for ease of rendition, the unit cell origin is shifted by 1/2 1/2 1/2 relative to the coordinates given in Table 2. In (a), the small red spheres are the Mo atoms and the large green spheres are N atoms, with half of the N sites randomly vacant. In (b), the small central red sphere is the Mo(1) atom on the 1a site, the small yellow spheres are the Mo(2) atoms on the 3c site, the large green atoms are the N(1)/O(1) atoms on the 1b site, and the large blue atoms are the N(2)/O(2) atoms on the 3d site.

refinement results (Table 2) show that while the 1a and 3c sites host the Mo cations, the site occupancies of these two sites differ in both A800 and A700. Analogous distinctions are evident for the 1b and 3d sites on which the anions reside. In A700, the 1b site is preferentially occupied by oxygen, and the 3d site by nitrogen. Because of the high correlation between site occupancies, chemical identity, and displacement parameters, the final refinement was carried out assuming complete site differentiation, full site occupancies, and equal displacement parameters at these two sites following refinement results that supported such an assignment. Realistically, some site mixing would be expected, but model insensitivity precluded precise determination of this effect. In contrast to A700, in A800, the 1b site is nearly entirely vacant, and the few anions residing on this site are nitrogen species. The 3d site is predominantly occupied by nitrogen species, and in this feature, A800 and A700 are similar. Again because of the high correlation between relevant parameters, the final refinement was performed taking the 3d site to be fully occupied. Free refinement consistently resulted in an occupancy factor exceeding 1. The appearance of X-ray and electron superstructure peaks in A800 and not in A700 reflects the nature of the vacancy ordering on the cation sites. Because of the lower site multiplicity of the 1a sites, the presence of Mo vacancies on this site (A700) does not generate superstructure peak intensity at a level comparable to that generated by vacancies on the 3c site (A800). The NPD patterns, on the other hand, reveal superstructure peaks largely as a result of the anion distribution, with oxygen and nitrogen nearly fully ordered in A700 and vacancies and nitrogen species nearly fully ordered in A800. Although the structure refinement is not particularly sensitive to the low oxygen occupancy on the 3d site, the features of the A800 oxygen ELNES spectrum (Figure S3b) support the conclusion that bulk oxygen is present in the material. At the same time, the greater similarity of the A800 oxygen ELNES spectrum to those of the molybdenum oxides as compared to that of A700 suggests a larger relative contribution of surface oxides to the spectroscopy measurement in A800, consistent with the low bulk oxygen concentration. The presence of hydrogen, the locations of which were not resolved, also presumably contributes to the NPD superstructure peak intensities, particularly those of A700. The greater breadth of the superstructure peaks compared to those of the substructure suggests that the site ordering is spatially limited and does not extend over the entire length of the crystallites. The final weighted residuals from the refinements (wRp) were 5.95% and 9.55% for A700 and A800, respectively (Table 2).

In general agreement with the diffraction data, the EXAFS analysis (Table S2) showed the local coordination environment about the Mo in A700 to be formed of species located at distances of 2.15(3) and 2.88(12) Å from the central Mo atom. These correspond to the Mo–O/N and the Mo–Mo distances determined from the refinement to be 2.09213(4) and 2.95872(6) Å, respectively. That the Mo–anion distance is single-valued suggests that there are no distinct oxygen-rich or nitrogen-rich regions in the material. In the case of A800, a nearest-neighbor distance of 2.11(3) Å is found from EXAFS, again corresponding to the Mo–O/N distance, where the anions in this case are predominantly N. The slight contraction relative to A700, despite a larger lattice constant in A800, suggests local distortions in which the atoms are displaced from the high symmetry positions. Such distortions are

strongly indicated by the detection of two apparent Mo–Mo distances in the EXAFS analysis, 2.64(2) and 2.91(7) Å. Furthermore, slight discrepancies between the measured and calculated diffraction patterns of A800 indicate shortcomings of the solution to the A800 structure, which implies a single Mo–Mo distance of 2.98508(5) Å. Structure refinements in which the Mo atoms were moved off from their respective 1a and 3c sites were attempted but did not produce satisfactory results. Alternatively, a lower symmetry in this material may be possible, but the narrowing of peaks relative to A700 argues against a lowering of the crystal class. Refinement in the space group $P4/mmm$ (results omitted for brevity) produced only marginally better refinement statistics along with a large disagreement with the measured stoichiometry. Thus, while the general structure of A800 has been captured, the resolution of the finer details awaits more focused investigations. Such studies may also explain the surprisingly low coordination numbers determined from the EXAFS analysis for both phases (Table S2).

The final compositions derived from the refinements were $\text{Mo}_{0.775(2)}(\text{N}_{0.75}, \text{O}_{0.25})$ for A700 and $\text{Mo}_{0.790(1)}(\text{N}_{0.729(5)}, \text{O}_{0.062(1)})$ for A800, which are in general agreement with the chemical analysis. In particular, the structure analysis captures the higher anion/cation ratio in A700 than that in A800. Furthermore, taking the nitrogen and oxygen valences as -3 and -2 , respectively, the average oxidation states of Mo in the two materials are ≈ 3.5 and ≈ 2.9 , respectively, in good agreement with the oxidation state of ≈ 3 obtained from the XPS analysis and the conclusion of a higher Mo oxidation state in A700 arrived at from the EELS measurements. The chemical formulas noted above are written to specify the mean vacancy concentrations over the two Mo sites, the absence of vacancies on the anion sites of A700, and their presence in A800. The densities implied by the compositions, $8.06(2) \text{ g cm}^{-3}$ (A700) and $7.68(1) \text{ g cm}^{-3}$ (A800), are much larger than those measured by pycnometry (Table 1). The discrepancy suggests that indeed the materials contain a large volume of closed porosity in addition to the vacancies detected by diffraction and EXAFS analysis. The higher diffraction density and lower pycnometry density of A700 suggest that this material has a higher internal porosity than A800, which is consistent with its higher specific surface area and morphology (Figure 1).

3. DISCUSSION

The overall features of the A700/A800 structures are presented in Figure 7 along with a comparison to the standard $Pm\bar{3}m$ structure typically reported for “ Mo_2N ”. For clarity, the mixed and partial occupancies are not directly indicated in the figures. Renditions of the structures presenting these details are provided in Figure S12. As noted above, the $Pm\bar{3}m$ space group occurs in A700/A800 because the translational symmetry required for $Fm\bar{3}m$ is lost as a consequence of the distinction of the chemical species residing on the 1a, 3c and 1b, 3d pairs of sites, which host the cation and anion species, respectively. In conventional “ Mo_2N ”, Mo fully occupies the cation sites, creating translational symmetry between 1a and 3c sites, and N partially occupies the anion sites, with randomly distributed vacancies, creating translational symmetry between 1b and 3d sites. The distinction between the A700 and A800 structures arises from the manner in which these pairs of sites are differentiated. In A700, vacancies occur on both of the Mo sites, whereas in A800, the 1a site on which Mo(1) resides is fully occupied and the 3b site of Mo(2) is almost 30% vacant.

The distribution of anions differs even more strongly between A700 and A800 than the distribution of cations. In particular, the 1b site is almost entirely unoccupied in A800, whereas it is fully occupied by oxygen in A700. The 3d site, however, is fully occupied in both materials, either entirely or primarily by nitrogen. Notably, oxygen is incorporated into the site of a higher coordination number in both materials (Table 2), where the coordination numbers differ from 6 because of the partial occupancies on the cation sites. The occupancies on the cation 3c sites translate into mean anion coordination numbers on the 1b site of ≈ 5.1 and ≈ 4.3 in A700 and A800, respectively. Analogously, the mean anion coordination numbers on the 3d site, coordinated by Mo atoms on both the 1a and 3c sites, correspond to coordination numbers of ≈ 4.5 and ≈ 4.9 , respectively. The large difference in the oxygen ELNES of A700 and A800 (Figure 3b) suggests differences in the coordination environment, beyond the moderate difference in the coordination number of the oxygen species derived from the refinement (5.1 vs 4.9).

While H atoms could not be reliably located, their presence in the materials was definitively established by the chemical analysis. It is likely that these species are present as protons as Pande et al. have showed by XANES that electrochemical insertion of H into molybdenum nitride induces a slight reduction of Mo.³⁹ The source of H in the present materials is assumed here to be the ammonia used in the nitridation. In particular, it is known that an orthorhombic molybdenum bronze (H_xMoO_3) forms along the reaction pathway between MoO_3 and NH_3 to produce molybdenum nitrides.^{19,20,40,41} Such protons are apparently retained in the cubic phases.

Beyond a distinction in overall chemistry, the two materials studied here show a slight difference in the lattice constant, with that of A700 being somewhat smaller than that of A800. Such a result is also evident in the XRD patterns reported by Tagliazucca et al.³² The difference in cell volumes can plausibly be attributed to the significant presence of oxygen, with a smaller anionic radius than nitrogen, in the A700 material. The decrease in cell volume on heating under hydrogen (Figure 5) indicates that anions can be lost from the structures without a complete collapse of the framework. The contraction of A700 further implies a chemical change in this material in a manner that retains its chemical distinction from A800. Thus, loss of oxygen and that of nitrogen likely occur simultaneously, as opposed to the preferential loss of oxygen. It is of some note that Tagliazucca et al.³² also reported a cell contraction at a high temperature of their " $Pm\bar{3}m Mo_xN_y$ ", but in this case upon exposure to NH_3 rather than hydrogen, and with a slightly higher onset temperature of ≈ 823 K.

Based on the structure determinations, a hypothesis for the mechanism by which the A800 phase forms emerges. We first presume that the A700 structure appears along the pathway to forming the A800 phase, rather than a direct formation of the A800 material from some other precursor state. The transformation from A700 to A800 then corresponds to a loss of O and H, and, to a small extent, N, from the structure to generate a near-stoichiometric material. The release of oxygen from the structure is accompanied by a shift in the Mo position from preferential occupation of the 3c site to preferential occupation of the 1a site, as well as the creation of a notable concentration of anion vacancies. The average cation vacancy concentration, on the other hand, remains relatively unchanged. The loss of surface area and apparent loss of

internal porosity in A800 are the result of high temperature coarsening.

The results obtained here for the chemistries and structures of molybdenum nitride materials prepared by ammonolysis of MoO_3 are quite distinct from what is typically reported. In particular, we find that regardless of the synthesis temperature (973 or 1073 K), the material is anion-rich relative to " Mo_2N ," the cation vacancy concentrations are substantial, and the space group symmetry is $Pm\bar{3}m$ rather than $Fm\bar{3}m$. The key chemical distinction imparted by varying synthesis temperature is the extent to which oxygen is retained, which then establishes the overall anion-to-cation ratio. In prior studies, the difficulty of distinguishing N and O by XRD and electron diffraction has undoubtedly obscured the anion ordering that gives rise to the space group $Pm\bar{3}m$ for materials produced at moderate ammonolysis temperatures of ≈ 973 K. Furthermore, anion chemical analysis is relatively uncommon when the synthetic goal is the preparation of high surface area materials for catalytic studies, although some authors have detected the presence of residual oxygen.^{23,26} On the other hand, it is likely that small differences in synthesis conditions produce variations in anion-to-cation ratios, distinct concentrations of residual oxygen, and differing levels of anion ordering, even when the ammonolysis temperature is 973 K. Cao et al., for example, employed NPD to study materials similar to the A700 material prepared here and did not detect mixed parity superstructure peaks, although the possibility that the material was anion-rich relative to Mo_2N was acknowledged.¹² Furthermore, these authors observed a large incoherent background, attributed, as in this work, to the presence of hydrogen in the material. In contrast to synthesis at 973 K, ammonolysis of MoO_3 at higher temperatures has been previously recognized to produce materials of the space group $Pm\bar{3}m$, specifically, as noted above, by Tagliazucca et al.³² Notably, these authors concluded (apparently from the X-ray structure refinement) that the stoichiometry of their material was $Mo_{3.2}N_{2.7}$. No NPD studies or chemical analysis has been to date reported for this phase.

In general, the perception that the stoichiometry of cubic molybdenum nitride produced from MoO_3 contains more cations than anions is pervasive in the literature. This perception appears to derive from the reported behavior of oxygen-free Mo–N compounds, where it is known that stoichiometric MoN is thermodynamically more stable in a hexagonal form, the δ phase, than in the B1 rock salt structure.²⁹ However, even in true molybdenum nitrides, both computational⁴² and experimental⁴³ studies point toward the presence of vacancies on both cation and anion sites, with cation vacancies displaying more negative defect formation energies, as referenced to the hypothetical perfect B1 structure. Thus, detection, here, of materials with vacancies on the cation sites is not unreasonable. Most importantly, the comprehensive chemical analysis performed here permits no other conclusion than an anion-rich stoichiometry in materials produced by ammonolysis at the most commonly used synthesis temperature of 973 K.

4. CONCLUSIONS

Temperature-programmed ammonolysis of MoO_3 at 973 and 1073 K was used to prepare nitrated products of cubic symmetry. While typically considered to adopt an anion-deficient MoN_x rock salt structure, we find that the materials obtained by this process are in fact hydrogen-incorporated,

molybdenum oxynitrides of general stoichiometry $\text{Mo}_{1-x}(\text{N}_{1-y}\text{O}_y)\text{H}_z$. We highlight the limitations of using XRD and/or electron diffraction for determining the structures of these complex systems. In particular, these techniques are unable to detect the co-occupation of anion sites by O along with N. Here, the true structures and compositions are revealed by the Rietveld corefinement using both powder ND and XRD data and by quantitative chemical analysis with the data from PGAA, combustion analysis, and TGA. Both materials crystallize in the space group $Pm\bar{3}m$ and do not display the translational symmetry inherent to the $Fm\bar{3}m$ space group of the rock salt prototype structure. The two crystallographically distinct cation sites in the $Pm\bar{3}m$ structure have distinct occupancy factors, with a relatively large difference in the case of the material synthesized at 1073 K. Accordingly, superstructure peaks with indices of mixed parity are evident in the XRD and the electron diffraction patterns of this material. Such peaks are absent in the patterns of the material synthesized at 973 K. Differences in the N and O occupancies on the two occupied anion sites are also observed and give rise to the NPD superstructure peaks. The composition deduced for the material synthesized at 973 K is $\text{Mo}_{0.775(2)}(\text{N}_{0.75}, \text{O}_{0.25})$, whereas that for the material synthesized at 1073 K is $\text{Mo}_{0.790(1)}(\text{N}_{0.729(5)}, \text{O}_{0.062(1)})$. Thus, about one-fourth of the anion content is due to oxygen under typical preparation conditions, whereas reaction at higher temperatures results in a substantially lower oxygen concentration. The high temperature transformation to a stoichiometry richer in cations (upon synthesis at 1073 K as compared to synthesis at 973 K) is accompanied by an expansion of the lattice, a preferential shift of the Mo atoms from one cation site to another, loss of specific surface area, and an increase in pycnometry-measured density. Furthermore, sites formerly nearly fully occupied by oxygen become nearly fully vacant, while the shift in the Mo position results in preferential coordination by the cations of the oxygen-bearing anion sites in both structures. The transformation is also accompanied by a slight decrease in the Mo oxidation state, as detected by both EELS and XANES measurements. The sum of these observations suggest that cation-deficient, rock salt “molybdenum nitride” (A700) is stabilized by the incorporation of oxygen, whereas the nearly stoichiometric analog (A800) is stabilized by ordered vacancies on the anion sites.

These comprehensive studies form a critical first step in establishing the extent of the chemical tunability of the $Pm\bar{3}m$ molybdenum oxynitride phase. Chemical tunability may, in turn, enable precise control of the catalytic and electronic properties of $\text{Mo}_{1-x}(\text{N}_{1-y}\text{O}_y)\text{H}_z$.

5. MATERIALS AND METHODS

Samples were prepared by temperature-programmed ammonolysis of MoO_3 . For each synthesis, 0.25 g of MoO_3 (99.9995% metals basis, Alfa Aesar, or 99.97% metals basis, Sigma-Aldrich) was placed inside a tube furnace at ambient temperature and immediately subjected to a flow of 100 mL min^{-1} (space velocity of 1.65 cm s^{-1}) of anhydrous NH_3 . The material was then subjected to the following thermal profile: heat to 623 K (5 K min^{-1} , no hold), heat to 773 K (0.6 K min^{-1} , no hold), heat to either 973 or 1073 K (3 K min^{-1} , 3 h hold), and finally furnace-cool to ambient temperature while still under ammonia flow. The majority of the experiments were performed using the higher purity Alfa Aesar precursor. As described below, some sample-to-sample variations in physical characteristics were observed. Because of the limitations of the sample mass in the synthesis, not all characterization studies could be performed on a single batch of

materials, and in some cases, multiple batches were combined. Variability in the results is assessed via duplicate measurements.

The sample morphology was studied by SEM in secondary electron imaging mode using a Hitachi SU8030 equipped with a cold-field emission source operating at 15 kV and $10 \mu\text{A}$. No prior coating was necessary given the conducting nature of the samples. BET surface areas and the pore(s) size were determined from nitrogen physisorption isotherms measured at liquid nitrogen temperature using a Micromeritics 3Flex instrument and samples 50–200 mg in mass. Data were analyzed using the MicroActiv software package, which provides quantitative uncertainty estimates for the surface area. The uncertainty in the pore-size determination was taken to be 1 in the final digit obtained from the analysis. Phase formation was evaluated by laboratory XRD (Ultima, Rigaku) using Cu $K\alpha$ radiation at a scan rate of $2.5^\circ \text{ min}^{-1}$ with a step size of 0.05° . The sample was ground, then placed on a zero background SiC holder, and rotated at a speed of 3.1 rad s^{-1} during measurement. The commercial software package, JADE (MDI Inc.), was used for whole pattern fitting to determine the lattice constant and the crystallite size along with their uncertainties. For the purposes of this analysis, the entirety of the peak broadening was attributed to size effects. A Micromeritics AccuPyc II 1340 pycnometer was utilized for the density determinations of all samples. Between 50 and 400 mg of the sample was loaded into an aluminum cap (1 mL), and the volume was determined on the basis of He displacement. The volume of each sample was measured three times, and the standard deviation was recorded along with the average volume. The measured masses (obtained using an analytical balance) were then used for the density calculations. The estimated standard deviation was obtained from the range in values across the three measurements.

For TEM and EELS studies, powder products were lightly ground, sonicated in ethanol, and dropped on ultrathin carbon-coated Cu grids. Conventional TEM images and SAED patterns were obtained using a JEOL Grand ARM 300F operated at 300 kV. STEM images and EELS spectra were acquired at 200 kV using a Cs-corrected JEOL ARM 200CF equipped with a Quantum Dual EELS system. EELS spectra of the two samples were obtained from areas with similar thickness. The thicknesses were estimated from the zero-loss spectra, which showed t/λ values of 0.45 and 0.40 for the A700 and A800 samples, respectively.

Core-loss and low-loss EELS spectra were collected using an entrance aperture of 5 mm and an energy dispersion of 0.25 eV/channel, which resulted in a 1.5 eV energy resolution. The convergence angle was set to 20.6 mrad, and the probe size was $\approx 2 \text{ \AA}$. STEM/EELS data sets were collected using the commercial software package Gatan Microscopy Suite (GMS). The simultaneous acquisitions from multiple channels were synchronized using the Gatan Digiscan system. Final EELS spectra were obtained by averaging the signal across different areas within the sample. Simultaneous acquisition of core-loss spectra and low-loss spectra enabled accurate measurement of absolute chemical shifts and energy differences.⁴⁴ Data analysis was performed with GMS and the commercial software package Origin. For EELS analysis, core-loss spectra were aligned using simultaneously acquired low-loss spectra. Background subtraction was then performed on both spectra using a power law expression, AE^{-r} , where E is energy and A and r are constants, in the pre-edge energy window 180–220 eV. Multiple scattering effects were removed by Fourier-ratio deconvolution following the methods described by Egerton.⁴⁵ The $\text{Mo}_{\text{M},2,3}$ and N_{K} edges overlap at around 400 eV, and the features were thus deconvoluted by peak fitting to obtain peak energies. The uncertainty in the energy onset position in EELS is reflected in the nature of zero loss peak (ZLP), which embodies the point-spread-function of the EELS spectrometer, all instrument/acquisition instabilities, and related perturbations to the energy onset position. As a result, some fraction of the width of the ZLP is often considered as the uncertainty in EELS. That fraction is, in turn, determined by the ability of modern curve-fit software and other methods to discriminate or identify overlapped edges, which is conservatively one-third of the ZLP width

(and optimistically 1/5).⁴⁵ Thus, with a ZLP of about 1.5 eV (with sample in the beam), the energy uncertainty is ≈ 0.4 eV.

Qualitative chemical analysis was performed by XPS using a Thermo Scientific ESCALAB 250Xi instrument, equipped with an aluminum anode (Al $K\alpha = 1486.6$ eV) X-ray source, an electron flood gun, a scanning ion gun, and a heating stage. Samples were prepared by pressing the ammonolysis products into a disc, 3.2 mm in diameter. Because Ar etching, which is typically used to remove surface species, is known to modify the Mo oxidation state in molybdenum bearing compounds,³⁶ the contribution of adsorbed gases to the signal (potentially N_2 , H_2O , NH_3 , and H_2) was minimized by performing measurements at elevated temperatures. Once inside the preparation chamber, the sample was slowly heated to 523 K and held until the vacuum-stabilized at $\approx 1.3 \times 10^{-5}$ Pa, approximately 45 min. Following an initial survey scan (not shown), which revealed the presence of Mo, N, and O in the oxynitride samples, high-resolution data were collected in the Mo 3d (220–240 eV), C 1s (279–298 eV), and O 1s (520–545 eV) regions using a step size of 0.1 eV with a dwell time of 50 ms and integrating over 10 scans. Due to significant peak overlap, results in the N 1s–Mo 3p region (380–405 eV) are not reported. Charging effects were corrected by referencing to the adventitious carbon C 1s binding energy (BE) at 284.8 eV. The commercial software package Thermo Scientific Avantage was used for data processing. The instrument energy resolution of 0.10 eV was taken as the uncertainty in the binding energies determined by this analysis. The attributes of the Mo 3d XPS peaks were established by fitting doublets with standard constraints (Mo 3d_{5/2} and Mo 3d_{3/2} with intensity ratio 3/2 and $\Delta BE \approx 3.15$ eV; Figure S4 and Table S1). Peaks due to three species were resolved: Mo⁶⁺ at a BE of $\approx 232.6(1)$ eV, Mo⁴⁺ at a BE of $\approx 230.1(1)$ eV, and Mo^{δ+} at a higher BE, with the assignments based on the literature studies of molybdenum oxides.^{17,37,46}

Quantitative and semiquantitative chemical analyses were performed using a combination of TGA, combustion analysis, and PGAA. Uncertainty in the analysis stems from the variable extent of surface oxidation/hydration.²⁴ To mitigate against this factor, characterization experiments were generally performed within a few days of sample synthesis. TGA was used in complete reduction experiments to reveal the total mass of Mo in the materials and thereby provides an estimate of the anion-to-cation ratio. Data were collected using a Netzsch STA F3, using 50–75 mg of ground powder in each measurement. The sample was loaded into a Pt pan, heated to 1173 K under 3% H_2 (balance Ar) or 7% H_2 (balance He) at a rate of 2 K min^{-1} , and held for 3 h. Laboratory XRD was performed after completion of the TGA experiment to confirm, within detection limits, the presence of only the Mo metal in the reduction product. The uncertainty in the TGA mass measurements was determined from the manufacturer-reported instrument drift (5 $\mu g h^{-1}$), in combination with the sample mass and the total measurement time. This uncertainty was smaller than the sample-to-sample variation in mass loss. The onset of bulk mass loss was tracked by in situ XRD under flowing 7% H_2 (balance He) using an Anton Paar XRK 900 reactor chamber mounted on a 9 kW Cu rotating anode Rigaku Smartlab diffractometer (see the Supporting Information for further details). Determination of the nitrogen and in some cases hydrogen content was performed by microchemical combustion analysis using the commercial service of Midwest Microlabs. The materials were examined in either the as-synthesized state or after heat-treatment under Ar at 673 K to remove surface-adsorbed species, a step that typically resulted in a 2–3% decrease in mass. For the analysis, samples were combusted at 1273 K under ultrapure oxygen, and the effluent stream was evaluated to determine the nitrogen and steam content. In principle, the absolute oxygen content can be determined through an analogous pyrolysis approach, but the facility was unable to perform such a measurement. Uncertainties in the N and H mass fractions so determined are as provided by Midwest Microlabs.

PGAA measurements were carried out at the cold neutron PGAA instrument at neutron guide D at the NIST Center for Neutron Research. A pressed pellet weighing approximately 300 mg was prepared from as-synthesized samples of each material using a 13 mm

diameter die and a hydraulic press. Calibration standards were prepared from mixtures of MoO_3 (99.9995% metals basis, Alfa Aesar) with urea (SRM 912b) and graphite (Spectrographic Services, 100 mesh), MoO_2 (99% metal basis, Alfa Aesar) with the aforementioned urea and graphite, and ammonium molybdate tetrahydrate (ACS reagent grade, 81.0–83.0% MoO_3 basis, Fisher Scientific), with the mixture or compound being pressed into a 300 mg pellet to give the same geometry as the A700 and A800 samples. For PGAA analysis, samples and standards were packaged in Al foil and were irradiated in vacuum inside a ⁶Li–aluminum lined sample box. The prompt gamma-ray emissions at 778 keV (Mo), 2223 keV (H), and 10 830 keV and its two escape peaks at 10 318 keV and 9807 keV (N) were detected using an n-type, closed-end, coaxial high-purity germanium (HPGe) detector (41% efficiency) surrounded by a bismuth germanate Compton shield.^{47–49} Oxygen has an extremely low prompt gamma-ray cross section, rendering quantification of this element by PGAA unfeasible. Mass ratios (mg/mg) for Mo/N and Mo/H were calculated using count rates from gamma rays measured in sample spectra and element sensitivities (counts $s^{-1} mg^{-1}$) calculated from gamma-ray count rates in standards spectra and from standards preparation data. These were converted to molar ratios using atomic mass data for Mo, N, and H. Relative 2σ uncertainties for the resulting Mo/N and Mo/H ratios were estimated at 2.5% based on the following (with approximate 1σ contribution): counting statistics (1%), standards measurement replication ($\frac{\sigma}{\bar{x}} = \frac{0.7}{\sqrt{n}}$ for the average Mo/N sensitivity ratio calculated for the three standards and $\frac{0.5}{\sqrt{3}}$ for the Mo/H ratio), purity of standards (estimated at 0.5%), and target positioning in the beam (estimated at 0.5% from repeated measurements of the gamma-ray count rate of a Ti flux monitor).

ND data were collected using the POWGEN instrument of the Spallation Neutron Source at Oak Ridge National Laboratory. Powder samples were loaded into vanadium cans, and diffraction patterns were measured from two detector banks at ambient temperature. Neutron Bank 1 (NB1) offers a higher TOF range (with moderate resolution), whereas Neutron Bank 2 (NB2) offers better resolution (with shorter range). The data from NB1 were analyzed over the TOF range from 8 to $76 \times 10^3 \mu s$, corresponding to a q range of 1.87 to 17.73 \AA^{-1} (d -spacing ≈ 0.35 – 3.36 \AA). NB2 data were analyzed in the TOF range of 11.6 – $76 \times 10^3 \mu s$ corresponding to a q range of 1.87 – 12.22 \AA^{-1} (d -spacing ≈ 0.51 – 3.36 \AA). X-ray synchrotron powder diffraction patterns were collected at beamline 11-BM of the Advanced Photon Source at Argonne National Laboratory. The measurements were performed at ambient temperature using an X-ray wavelength of 0.457876 \AA , with the sample placed in a capillary spun at ≈ 90 Hz. For A700, data were analyzed from 7.96° to 46° in 2θ , implying a q range of 1.90 – 10.65 \AA^{-1} . For A800, the corresponding ranges were from 7.44° to 46° in 2θ and from 1.73 – 10.65 \AA^{-1} in q . The d -spacing ranges were thus 0.59 – 3.30 \AA (A700) and 0.59 – 3.52 \AA (A800). Lattice parameters, atomic coordinates, and atomic isotropic thermal parameters were obtained by combined Rietveld refinement of XRD and ND patterns using the General Structure Analysis System II package.⁵⁰ The backgrounds in the ND patterns were fitted with sixth-degree Chebyshev and Chebyshev-1 polynomials for A700 and A800, respectively, whereas for the XRD patterns, seventh-degree Chebyshev and fifth-degree Chebyshev-1 polynomials were used for A700 and A800, respectively. The scale factor, sample absorption, sample displacement perpendicular to the beam, crystallite size (isotropic for A700, uniaxial for A800), and microstrain (uniaxial) parameters were sequentially refined for each material. In the final respective final refinement cycles, seven independent crystal structure parameters were refined for A700 and eight for A800. In principle, hydrogen, which is entirely invisible to X-rays (and electrons) in the presence of Mo, is also detected by ND due to its negative scattering length of -3.7390 fm .³³ However, inclusion of this species at sites identified by difference Fourier maps produced only marginal improvements to the refinement statistics, and thus, hydrogen was omitted from the final refinements. The reported uncertainties are the statistical uncertainties obtained from

the GSAS refinements and, for derived quantities, from numerical propagation of such uncertainties.

The oxidation state and local structure were further probed by XAS, including both XANES and extended X-ray absorption fine structure (EXAFS) measurements. Experiments were performed at beamline SBM-D at the Advanced Photon Source at Argonne National Laboratory. Data were collected at the Mo K-edge (20 000 eV). Powder samples were uniformly spread on tape and measured in transmission mode. All samples were calibrated to a Mo metal foil measured in-line during each sample measurement. Data reduction and analysis were performed using the Demeter software package.⁵¹ Details of the EXAFS analysis methods are provided in the [Supporting Information](#).

■ ASSOCIATED CONTENT

SI Supporting Information

The Supporting Information is available free of charge at <https://pubs.acs.org/doi/10.1021/acs.chemmater.1c00617>.

Optical images of oxynitride products, SEM of MoO₃ precursor, EELS spectra and peak deconvolution, XPS Mo 3d spectra and peak deconvolution, TGA weight loss curves, PGAA spectra, and synchrotron X-ray diffraction and ND patterns ([PDF](#))

Crystallographic details of A700 ([CIF](#))

Crystallographic details of A800 ([CIF](#))

■ AUTHOR INFORMATION

Corresponding Authors

Vinayak P. Dravid – *Materials Science and Engineering, Northwestern University, Evanston, Illinois 60208, United States*; orcid.org/0000-0002-6007-3063; Email: v-dravid@northwestern.edu

Gabriela B. González – *Physics and Astrophysics, DePaul University, Chicago, Illinois 60614, United States*; Email: ggonza18@depaul.edu

Sossina M. Haile – *Materials Science and Engineering, Northwestern University, Evanston, Illinois 60208, United States*; orcid.org/0000-0002-5293-6252; Email: ssossina.haile@northwestern.edu

Authors

Shobhit A Pandey – *Materials Science and Engineering, Northwestern University, Evanston, Illinois 60208, United States*; orcid.org/0000-0002-4384-5463

Chi Zhang – *Materials Science and Engineering, Northwestern University, Evanston, Illinois 60208, United States*; orcid.org/0000-0002-6116-5437

Daniah H. Ibrahim – *Physics and Astrophysics, DePaul University, Chicago, Illinois 60614, United States*

Elise A Goldfine – *Materials Science and Engineering, Northwestern University, Evanston, Illinois 60208, United States*

Jill K. Wenderott – *Materials Science and Engineering, Northwestern University, Evanston, Illinois 60208, United States*

Roberto dos Reis – *Materials Science and Engineering, Northwestern University, Evanston, Illinois 60208, United States*

Rick L. Paul – *National Institute of Standards and Technology, Gaithersburg, Maryland 20899, United States*

Ioannis Spanopoulos – *Department of Chemistry, Northwestern University, Evanston, Illinois 60208, United States*; orcid.org/0000-0003-0861-1407

Mercouri Kanatzidis – *Department of Chemistry, Northwestern University, Evanston, Illinois 60208, United States*; orcid.org/0000-0003-2037-4168

Michael J. Bedzyk – *Materials Science and Engineering, Northwestern University, Evanston, Illinois 60208, United States*; orcid.org/0000-0002-1026-4558

Complete contact information is available at: <https://pubs.acs.org/doi/10.1021/acs.chemmater.1c00617>

Notes

The authors declare no competing financial interest.

■ ACKNOWLEDGMENTS

MRSEC-IRG2 (NSF, no. DMR-1720139) is acknowledged for financial support of this work. This work made use of the J.B. Cohen X-Ray Diffraction Facility for lab XRD. EPIC and Keck-II facilities of Northwestern University's NUANCE Center were used for TEM, SEM, and XPS analysis, which have received support from the SHyNE Resource (NSF, no. ECCS-2025633), the IIN, and the Northwestern University's MRSEC program (NSF, no. DMR-1720139). The CleanCat Core facility at the REACT center of Northwestern University was used for BET measurements. Heather Chen-Mayer from the NIST is acknowledged for assistance with PGAA data analysis. Midwest Microlabs is acknowledged for combustion analysis. Use of the Advanced Photon Source at Argonne National Laboratory was supported by the U.S. Department of Energy, Office of Science, Office of Basic Energy Sciences, under Contract no. DE-AC02-06CH11357. Synchrotron diffraction data were collected at the APS beamline 11 BM using the mail-in program.⁵⁰ A portion of this research used resources at the Spallation Neutron Source, a DOE Office of Science User Facility operated by the Oak Ridge National Laboratory, under Contract no. DE-AC05 00OR22725. Neutron diffraction data were collected at POWGEN using the mail-in program. Commercial products are mentioned only to specify the procedure in sufficient detail. Their inclusion in the paper does not imply product endorsement, nor does it imply that the mentioned products are the best for such use.

■ ABBREVIATIONS

XPS	X-ray photoelectron spectroscopy
EELS	electron energy loss spectroscopy
SAED	selected area electron diffraction
ELNES	energy loss near-edge structure
TGA	thermogravimetric analysis
PGAA	prompt gamma-ray neutron activation analysis
XRD	X-ray diffraction
ND	neutron diffraction
S/TEM	scanning/transmission electron microscopy
XAS	X-ray absorption spectroscopy
XANES	X-ray absorption near-edge spectroscopy
EXAFS	extended X-ray absorption fine structure.

■ REFERENCES

- (1) Rasaki, S. A.; Zhang, B.; Anbalgam, K.; Thomas, T.; Yang, M. Synthesis and application of nano-structured metal nitrides and carbides: A review. *Prog. Solid State Chem.* **2018**, *50*, 1–15.
- (2) Afify, H. H.; Hassan, S. A.; Abouelsayed, A.; Demian, S. E.; Zayed, H. A. Synthesis, characterization and structural control of nano crystalline molybdenum oxide MoO₃ single phase by low cost technique. *Mater. Chem. Phys.* **2016**, *176*, 87–95.

- (3) Aika, K.-I.; Ozaki, A. Mechanism and isotope effect in ammonia synthesis over molybdenum nitride. *J. Catal.* **1969**, *14*, 311–321.
- (4) Hargreaves, J. S. J. Nitrides as ammonia synthesis catalysts and as potential nitrogen transfer reagents. *Appl. Petrochem. Res.* **2014**, *4*, 3–10.
- (5) McKay, D.; Hargreaves, J. S. J.; Rico, J. L.; Rivera, J. L.; Sun, X. L. The influence of phase and morphology of molybdenum nitrides on ammonia synthesis activity and reduction characteristics. *J. Solid State Chem.* **2008**, *181*, 325–333.
- (6) Volpe, L.; Boudart, M. Ammonia Synthesis on Molybdenum Nitride. *J. Phys. Chem.* **1986**, *90*, 4874.
- (7) Wyvratt, B. M.; Gaudet, J. R.; Pardue, D. B.; Marton, A.; Rudić, S.; Mader, E. A.; Cundari, T. R.; Mayer, J. M.; Thompson, L. T. Reactivity of Hydrogen on and in Nanostructured Molybdenum Nitride: Crotonaldehyde Hydrogenation. *ACS Catal.* **2016**, *6*, 5797–5806.
- (8) Cao, B.; Veith, G. M.; Neuefeind, J. C.; Adzic, R. R.; Khalifah, P. G. Mixed close-packed cobalt molybdenum nitrides as non-noble metal electrocatalysts for the hydrogen evolution reaction. *J. Am. Chem. Soc.* **2013**, *135*, 19186–19192.
- (9) Chen, W. F.; Sasaki, K.; Ma, C.; Frenkel, A. I.; Marinkovic, N.; Muckerman, J. T.; Zhu, Y.; Adzic, R. R. Hydrogen-evolution catalysts based on non-noble metal nickel-molybdenum nitride nanosheets. *Angew. Chem., Int. Ed. Engl.* **2012**, *51*, 6131–6135.
- (10) Morozan, A.; Goellner, V.; Zitolo, A.; Fonda, E.; Donnadiu, B.; Jones, D.; Jaouen, F. Synergy between molybdenum nitride and gold leading to platinum-like activity for hydrogen evolution. *Phys. Chem. Chem. Phys.* **2015**, *17*, 4047–4053.
- (11) Ma, L.; Ting, L. R. L.; Molinari, V.; Giordano, C.; Yeo, B. S. Efficient hydrogen evolution reaction catalyzed by molybdenum carbide and molybdenum nitride nanocatalysts synthesized via the urea glass route. *J. Mater. Chem. A* **2015**, *3*, 8361–8368.
- (12) Cao, B.; Neuefeind, J. C.; Adzic, R. R.; Khalifah, P. G. Molybdenum nitrides as oxygen reduction reaction catalysts: Structural and electrochemical studies. *Inorg. Chem.* **2015**, *54*, 2128–2136.
- (13) Lee, K.-H.; Lee, Y.-W.; Kwak, D.-H.; Moon, J.-S.; Park, A.-R.; Hwang, E.-T.; Park, K.-W. Single-crystalline mesoporous Mo₂N nanobelts with an enhanced electrocatalytic activity for oxygen reduction reaction. *Mater. Lett.* **2014**, *124*, 231–234.
- (14) Pan, X.; Song, X.; Lin, S.; Bi, K.; Hao, Y.; Du, Y.; Liu, J.; Fan, D.; Wang, Y.; Lei, M. A facile route to graphite-tungsten nitride and graphite-molybdenum nitride nanocomposites and their ORR performances. *Ceram. Int.* **2016**, *42*, 16017–16022.
- (15) Sun, T.; Wu, Q.; Che, R.; Bu, Y.; Jiang, Y.; Li, Y.; Yang, L.; Wang, X.; Hu, Z. Alloyed Co–Mo Nitride as High-Performance Electrocatalyst for Oxygen Reduction in Acidic Medium. *ACS Catal.* **2015**, *5*, 1857–1862.
- (16) Li, X.-L.; Xing, Y.; Wang, H.; Wang, H.-L.; Wang, W.-D.; Chen, X.-Y. Synthesis and characterization of uniform nanoparticles of γ -Mo₂N for supercapacitors. *Trans. Nonferrous Met. Soc. China* **2009**, *19*, 620–625.
- (17) Ruan, D.; Lin, R.; Jiang, K.; Yu, X.; Zhu, Y.; Fu, Y.; Wang, Z.; Yan, H.; Mai, W. High-Performance Porous Molybdenum Oxynitride Based Fiber Supercapacitors. *ACS Appl. Mater. Interfaces* **2017**, *9*, 29699–29706.
- (18) Wu, H.; Lian, K. The Development of Pseudocapacitive Molybdenum Oxynitride Electrodes for Supercapacitors. *ECS Trans.* **2014**, *58*, 67–75.
- (19) Volpe, L.; Boudart, M. Compounds of Molybdenum and Tungsten with High Specific Surface Area. *J. Solid State Chem.* **1985**, *59*, 332.
- (20) Choi, J.-G.; Curl, R. L.; Thompson, L. T. Molybdenum nitride catalysts: I. Influence of the synthesis factors on structural properties. *J. Catal.* **1994**, *146*, 218–227.
- (21) Marchand, R.; Gouin, X.; Tessier, F.; Laurent, Y. New routes to molybdenum nitrides and oxynitrides: Preparation and characterization of new phases. In *The Chemistry of Transition Metal Carbides and Nitrides*; Oyama, S. T., Ed.; Springer, 1996.
- (22) Gates-Rector, S.; Blanton, T. The Powder Diffraction File: A quality materials characterization database. *Powder Diffr.* **2019**, *34*, 352–360.
- (23) Gouin, X.; Marchand, R.; L'Haridon, P.; Laurent, Y. Action de l'ammoniac sur l'oxyde de molybdène MoO₃. Caractérisation physico-chimique de la phase oxynitride de type Mo₂N. *J. Solid State Chem.* **1994**, *109*, 175–180.
- (24) Sayag, C.; Bugli, G.; Havil, P.; Djéga-Mariadassou, G. Surface Studies of Passivated Molybdenum Oxynitride. *J. Catal.* **1997**, *167*, 372–378.
- (25) Miga, K.; Stanczyk, K.; Sayag, C.; Brodzki, D.; Djéga-Mariadassou, G. Bifunctional Behavior of Bulk MoOxNy and Nitrided Supported NiMo Catalyst in Hydrodenitrogenation of Indole. *J. Catal.* **1999**, *183*, 63–68.
- (26) Lyutaya, M. D. Formation of nitrides of group 6 transition metals of the Periodic system. *Poroshk. Metall. (Kiev)* **1979**, *35*, 60–66.
- (27) Kreider, M. E.; Stevens, M. B.; Liu, Y.; Patel, A. M.; Statt, M. J.; Gibbons, B. M.; Gallo, A.; Ben-Naim, M.; Mehta, A.; Davis, R. C.; Ievlev, A. V.; Nørskov, J. K.; Sinclair, R.; King, L. A.; Jaramillo, T. F. Nitride or Oxynitride? Elucidating the Composition–Activity Relationships in Molybdenum Nitride Electrocatalysts for the Oxygen Reduction Reaction. *Chem. Mat.* **2020**, *32*, 2946–2960.
- (28) Bull, C. L.; Kawashima, T.; McMillan, P. F.; Machon, D.; Shebanova, O.; Daisenberger, D.; Soignard, E.; Takayama-Muromachi, E.; Chapon, L. C. Crystal structure and high-pressure properties of γ -Mo₂N determined by neutron powder diffraction and X-ray diffraction. *J. Solid State Chem.* **2006**, *179*, 1762–1767.
- (29) Jehn, H.; Ettmayer, P. The molybdenum-nitrogen phase diagram. *J. Less-Common Met.* **1978**, *58*, 85–98.
- (30) Balasubramanian, K.; Huang, L.; Gall, D. Phase stability and mechanical properties of Mo_{1-x}N_x with 0 ≤ x ≤ 1. *J. Appl. Phys.* **2017**, *122*, 19.
- (31) Troitskaya, N. V.; Pinsker, Z. G. On the cubic nitride of molybdenum. *Sov. Phys. Crystallogr.* **1959**, *4*, 33–36.
- (32) Tagliazucca, V.; Leoni, M.; Weidenthaler, C. Crystal structure and microstructural changes of molybdenum nitrides traced during catalytic reaction by in situ X-ray diffraction studies. *Phys. Chem. Chem. Phys.* **2014**, *16*, 6182–6188.
- (33) Sears, V. F. Neutron scattering lengths and cross sections. *Neutron News* **1992**, *3*, 26–37.
- (34) Jagers, C. H.; Michaels, J. N.; Stacy, A. M. Preparation of High-Surface-Area Transition-Metal Nitrides: Mo₂N and MoN. *Chem. Mater.* **1990**, *2*, 150.
- (35) Lajaunie, L.; Boucher, F.; Dessapt, R.; Moreau, P. Quantitative use of electron energy-loss spectroscopy Mo-M_{2,3} edges for the study of molybdenum oxides. *Ultramicroscopy* **2015**, *149*, 1–8.
- (36) Cowley, J. M.; Spence, J. C. H.; Smirnov, V. V. The enhancement of electron microscope resolution by use of atomic focusers. *Ultramicroscopy* **1997**, *68*, 135–148.
- (37) Choi, J. G.; Thompson, L. T. XPS study of as-prepared and reduced molybdenum oxides. *Appl. Surf. Sci.* **1996**, *93*, 143–149.
- (38) Statistical Descriptors of Crystallography. <http://ww1.iucr.org/iucr-top/comm/cnom/statdes/recomm.html> (accessed 31 July 2021).
- (39) Pande, P.; Deb, A.; Sleightholme, A. E. S.; Djire, A.; Rasmussen, P. G.; Penner-Hahn, J.; Thompson, L. T. Pseudocapacitive charge storage via hydrogen insertion for molybdenum nitrides. *J. Power Sources* **2015**, *289*, 154–159.
- (40) Zhang, Y.; Xin, Q.; Rodriguez-Ramos, I.; Guerrero-Ruiz, A. Temperature dependence of the pseudomorphic transformation of MoO₃ TO γ -Mo₂N. *Mater. Res. Bull.* **1999**, *34*, 145–156.
- (41) Dewangan, K.; Patil, S. S.; Joag, D. S.; More, M. A.; Gajbhiye, N. S. Topotactical Nitridation of α -MoO₃ Fibers to γ -Mo₂N Fibers and Its Field Emission Properties. *J. Phys. Chem. C* **2010**, *114*, 14710–14715.
- (42) Balasubramanian, K.; Khare, S. V.; Gall, D. Energetics of point defects in rocksalt structure transition metal nitrides: Thermodynamic reasons for deviations from stoichiometry. *Acta Mater.* **2018**, *159*, 77–88.

- (43) Ozsdolay, B. D.; Balasubramanian, K.; Gall, D. Cation and anion vacancies in cubic molybdenum nitride. *J. Alloys. Compd.* **2017**, *705*, 631–637.
- (44) Scott, J.; Thomas, P. J.; MacKenzie, M.; McFadzean, S.; Wilbrink, J.; Craven, A. J.; Nicholson, W. A. P. Near-simultaneous dual energy range EELS spectrum imaging. *Ultramicroscopy* **2008**, *108*, 1586–1594.
- (45) Egerton, R. F. *Electron Energy-Loss Spectroscopy in the Electron Microscope*, 3rd ed.; Springer: New York, NY, 2011.
- (46) Gruenert, W.; Stakheev, A. Y.; Feldhaus, R.; Anders, K.; Shpiro, E. S.; Minachev, K. M. Analysis of molybdenum(3d) XPS spectra of supported molybdenum catalysts: An alternative approach. *J. Phys. Chem.* **1991**, *95*, 1323–1328.
- (47) Paul, R. L.; Şahin, D.; Cook, J. C.; Brocker, C.; Lindstrom, R. M.; O'Kelly, D. J. NGD cold-neutron prompt gamma-ray activation analysis spectrometer at NIST. *J. Radioanal. Nucl. Chem.* **2014**, *304*, 189–193.
- (48) Turkoglu, D.; Chen-Mayer, H.; Paul, R.; Zeisler, R. Assessment of PGAA capability for low-level measurements of H in Ti alloys. *Analyst* **2017**, *142*, 3822–3829.
- (49) Popescu, G.; Herman, S.; Glover, S.; Spitz, H. Compton background suppression with a multi-element scintillation detector using high speed data acquisition and digital signal processing. *J. Radioanal. Nucl. Chem.* **2016**, *307*, 1949–1955.
- (50) Toby, B. H.; Von Dreele, R. B. GSAS-II: The genesis of a modern open-source all purpose crystallography software package. *J. Appl. Crystallogr.* **2013**, *46*, 544–549.
- (51) Ravel, B.; Newville, M. ATHENA, ARTEMIS, HEPHAESTUS: Data analysis for X-ray absorption spectroscopy using IFEFFIT. *J. Synchrotron Radiat.* **2005**, *12*, 537–541.